Strong magnetochiral dichroism for visible light emission in a rationally designed paramagnetic enantiopure molecule

Kouji Taniguchi,[1,2,*] Masaki Nishio,[3] Shuhei Kishiue,[2] Po-Jung Huang,[2] Shojiro Kimura,[1] and Hitoshi Miyasaka[1,2,†]

[1]*Institute for Materials Research, Tohoku University, 2-1-1 Katahira, Aoba-ku, Sendai 980–8577, Japan*
[2]*Department of Chemistry, Graduate School of Science, Tohoku University, 6-3 Aramaki-Aza-Aoba, Aoba-ku, Sendai 980–8578, Japan*
[3]*Department of Chemistry, Kanazawa University, Kakuma-machi, Kanazawa 920–1192, Japan*

Magnetochiral dichroism (MChD) in chiral materials is a nonreciprocal directional dichroism producing optical absorption/emission differences for unpolarized (or linearly polarized) light propagating parallel and antiparallel to a magnetic field; this is an intriguing optical phenomenon enabled by coupling between chirality and magnetism. Since ubiquitous unpolarized light can be coupled with chirality of materials in a magnetic field, MChD has been attracting attention as a potential source for asymmetric photochemical reactions and as an application source for novel magneto-optical devices. However, it has been weakly observed in the visible light region, which is of the order of $10^{-2}-10^{-1}\%$ for the corresponding signal, and prevents further applications. In this study, we demonstrate a strong MChD for visible light emission based on the microscopic mechanism in a terbium(III) chiral complex with highly symmetrical nona-coordinated geometry. The MChD signal reaches $\sim 16\%$ at 14 T of the luminescence intensity, involving the development of magnetization under magnetic fields.

I. INTRODUCTION

Since the time of Pasteur [1], the interplay between chirality and magnetism has become a popular topic in the fields of physics and materials science [2–4]. The relevant phenomena are, for example, known as a skyrmion with a topological spin texture in a chiral lattice [5], the spin-filtering effect by chiral molecules [6], and nonreciprocal directional light propagation in a chiral medium under magnetic fields, i.e., magnetochiral dichroism (MChD) [7–28]. Among them, MChD is experimentally observed as a difference of optical absorption or luminescence intensity for unpolarized (or linearly polarized) light, depending on parallel or antiparallel propagating direction to an applied magnetic field ($\boldsymbol{H}$). MChD depends on the sign of $\gamma^{R/L}\boldsymbol{k}\cdot\boldsymbol{H}(\gamma^{R}=-\gamma^{L})$, where $\gamma^{R/L}$ means chirality and $\boldsymbol{k}$ is a directional vector of light propagation. In particular, MChD for visible light is fascinating from the viewpoint of both fundamentals and applications, e.g., a fundamental scientific interest is to study the enantioselective photochemical reactions that might be initiated by ubiquitous visible solar light on earth [29,30], while applications are directed to the development of magneto-optical devices such as one-way transmission isolators driven without an additional polarizer [31]. However, a critical issue of MChD is that it has been very weakly detected in the visible light region. The reported MChD is of the order of $10^{-2}-10^{-1}\%$ for the corresponding signal [8–14], even in a ferromagnet where $H = 1.2$ T was applied [9].

In this work, we demonstrate strong MChD for visible light emission through a strategic molecular design based on the microscopic mechanism, in which MChD is described as the interference effect between electric dipole ($E1$) transition and magnetic dipole ($M1$) transition. The strong MChD signal was observed in paramagnetic chiral enantiomers of Tb^{3+} complexes with a large magnetic moment and a relatively highly symmetrical nona-coordinated geometry, $[Tb(L^{SS/RR})_3]X_3$ ($L^{SS/RR} = S$ or R-1-(2-naphthyl)ethylamine; $X = CF_3SO_3^-$, **$1^{SS/RR}$-Tb**; ClO_4^-, **$1'^{SS/RR}$-Tb**) [Figs. 1(a), 1(b), and Figs. S1, S2, and S3 in the Supplemental Material [41]]. Compounds **$1^{SS/RR}$-Tb** reveal a significant MChD signal of $\sim 6\%$ difference of the luminescence intensity at $H = 1$ T, and finally, the signal reaches $\sim 16\%$ at $H = 14$ T, exhibiting similar development with the magnetization originating from Tb^{3+} with $J = 6$ in the applied external magnetic field. This MChD of **$1^{SS/RR}$-Tb** is compared with those of isostructural Eu^{3+} complexes $[Eu(L^{SS/RR})_3](CF_3SO_3)_3$ (**$1^{SS/RR}$-Eu**) with $J = 0$ and another type of Tb^{3+}/Eu^{3+} complex with lower symmetrical local Tb^{3+}/Eu^{3+} coordination geometries [Figs. 1(c) and 3(b)]. The comparison of MChD signals have demonstrated that the observation of strong MChD is ascribed to a combination of two effects: (i) Zeeman splitting for M_J states in Tb^{3+} with $J \neq 0$; and (ii) a suppression of electric dipole transition ($E1$) by tuning the degree of inversion symmetry breaking in the local Tb^{3+} coordination geometry.

II. EXPERIMENTAL

A. Synthesis of chiral lanthanide complexes

The enantiomer complexes **$1^{SS/RR}$-Tb** and **$1'^{SS/RR}$-Tb**, which have different counter anions, $CF_3SO_3^-$ and ClO_4^-, were synthesized following a reported method for Eu compounds using $Tb(CF_3SO_3)_3$ and $Tb(ClO_4)_3$, respectively [32].

*taniguchi@imr.tohoku.ac.jp
†miyasaka@imr.tohoku.ac.jp
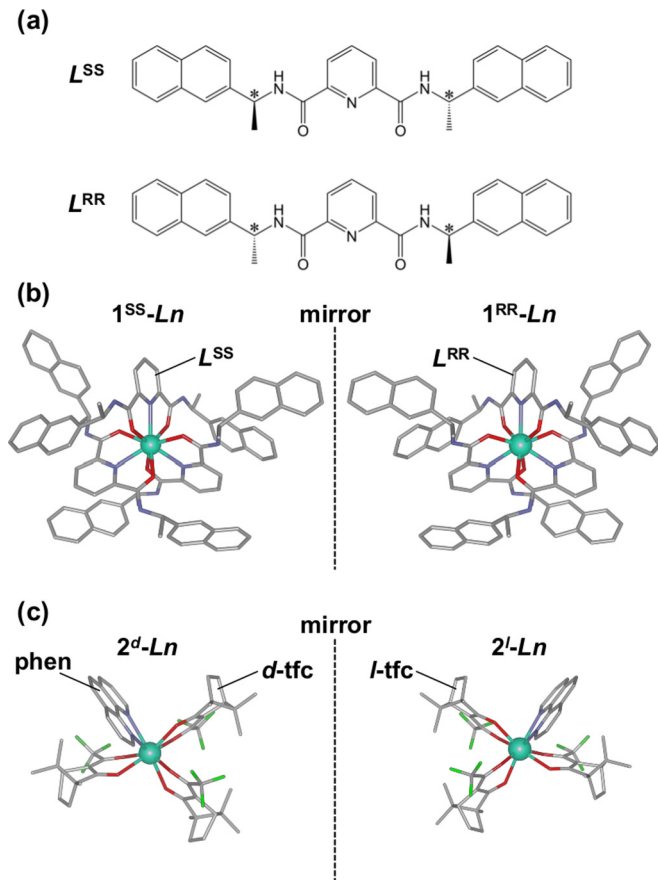
(a)

(b)

(c)

FIG. 1. Molecular structure of chiral lanthanide(III) complexes. (a) Schematic illustration of chiral ligands L^{SS} and L^{RR}. The asterisks represent asymmetric carbons. Enantiomer structures of chiral lanthanide ($Ln =$ Tb, Eu) complexes of (b) $1^{SS/RR}$-Ln and (c) $2^{d/l}$-Ln, where bluish green, red, blue, grey, and yellowish green represent Ln, O, N, C, and F, respectively. Hydrogen atoms are omitted for clarity.

The enantiopure chiral ligands $L^{SS/RR}$ [Fig. 1(a)] were prepared according to the method in Ref. [32]. To investigate the relationship between MChD and the magnetic ground state of lanthanide metal with $J \neq 0$ ($J = 6$ for Tb^{3+} with $^7F_6$), isostructural analogues of Eu^{3+} ($1^{SS/RR}$-Eu) with a nonmagnetic ground state ($J = 0$ for Eu^{3+} with $^7F_0$) were also prepared for comparison. In addition, to investigate the correlation between MChD and the symmetry of metal-around local coordination geometry (i.e., first coordination area for the metal center), another type of chiral Tb^{3+}/Eu^{3+} complex composed of three sets of 3-trifluoroacetyl-d/l-camphorato (d/l-tfc) and one 1,10-phenanthroline (phen), [$Ln(d/l$-tfc$)_3$(phen)] ($Ln =$ Tb, $2^{d/l}$-Tb; Eu, $2^{d/l}$-Eu) was also prepared according to the previously reported procedures for Eu compounds [Fig. 1(c)] [33–35]. The basic molecular structure of lanthanide complex in the series $1^{SS/RR}$-Ln was confirmed by single crystal x-ray diffraction analyses on $1'^{SS/RR}$-Tb (Tables S1 and S2 in the Supplemental Material [41]), to compare with the structures of [Eu($L^{SS/RR})_3$](ClO$_4)_3$ reported previously [32]. $2^{d/l}$-Tb and $2^{d/l}$-Eu were also structurally characterized (Tables S3, S4, and Fig. S4 in the Supplemental Material).

B. MChD measurement for luminescence in the visible light region

The measurements of MChD in luminescence were conducted for chiral terbium(III) and europium(III) complexes, which were dispersed in polymethyl methacrylate (PMMA) films. The film samples were placed in a cryostat equipped with a 15 T superconducting magnet at the High Field Laboratory for Superconducting Materials at Tohoku University (Fig. S5 in the Supplemental Material). Unpolarized ultraviolet (UV) light ($\lambda \leqslant 400$ nm) from a Xe lamp (Asahi Spectra MAX 301), in which the visible light component was cut by a mirror module and longpass filters, was focused on the sample for excitation of electronic states. The emitted light was collected in an optical fiber, which was set parallel to the direction of applied magnetic field. The intensity of emitted light was recorded by a spectrometer (Horiba JOBIN YVON iHR550) equipped with a CCD detector (ANDOR iDus DV401A). The magnetic field (H) was applied parallel or antiparallel to the propagation vector (k) of the emitted light (Fig. S5 in the Supplemental Material).

III. RESULTS AND DISCUSSION

A. Structural analysis

Enantiomer complexes of both $1'^{SS}$-Tb and $1'^{RR}$-Tb crystallize in the monoclinic space group $P2_1$ (Tables S1, S2, Figs. S2, and S3 in the Supplemental Material). Three chiral O-N-O trident ligands ($L^{SS/RR}$) isotropically coordinate with the Tb^{3+} ion, producing a relatively highly symmetrical nona-coordinated geometry, where the O-N-O coordinating atoms are composed of the central pyridine nitrogen atom and adjacent two oxygen atoms from the carboxamide group [Fig. 1(b)], and the complex molecules in $1'^{SS}$-Tb and $1'^{RR}$-Tb were isolated with Δ and Λ geometrical isomers, respectively (Fig. S1 in the Supplemental Material). Notably, $1'^{SS/RR}$-Tb were isostructural with their Eu^{3+} derivatives [32].

Enantiomer complexes of both 2^d-Tb and 2^l-Tb crystallize in the orthorhombic space group $P2_12_12_1$ (Tables S3 and S4 in the Supplemental Material). $2^{d/l}$-Tb is composed of heteroleptic ligands, three d/l-tfc and one phen [Fig. 1(c)], and the crystal field potential at Tb^{3+}-site is greatly deformed from the symmetric one compared with that of $1^{SS/RR}$-Tb [Figs. 1(b) and 3(a)] due to the presence of phen ligand [Figs. 1(c) and 3(b)]. The crystal structure of $2^{d/l}$-Eu was confirmed to be isostructural with that of $2^{d/l}$-Tb by measuring powder x-ray diffraction patterns (Fig. S4 in the Supplemental Material).

B. Magnetic characteristics

Reflecting the ground states of Tb^{3+} and Eu^{3+}, contrasting magnetic behavior was observed between 1^{SS}-Tb and 1^{SS}-Eu complexes. Figure 2(a) shows the temperature (T) dependence of the magnetic susceptibilities (χ) of 1^{SS}-Tb and 1^{SS}-Eu. The magnetic susceptibility of 1^{SS}-Tb, the ground state of which has a magnetic moment originated from $J = 6$ ($^7F_6$), increases with lowering temperature, while that of 1^{SS}-Eu displays almost temperature independent behavior with a small
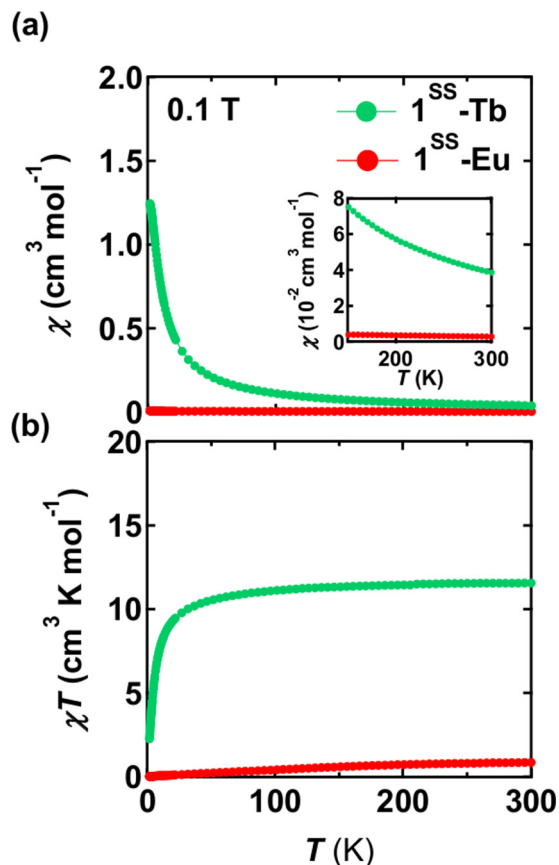
FIG. 2. (a) Temperature dependence of magnetic susceptibility (χ) of $\mathbf{1^{SS}}$-**Tb** (green circles) and $\mathbf{1^{SS}}$-**Eu** (red circles) in 0.1 T. The inset magnifies the high temperature range of χ. (b) Temperature dependences of χT for $\mathbf{1^{SS}}$-**Tb** (green circles) and $\mathbf{1^{SS}}$-**Eu** (red circles).
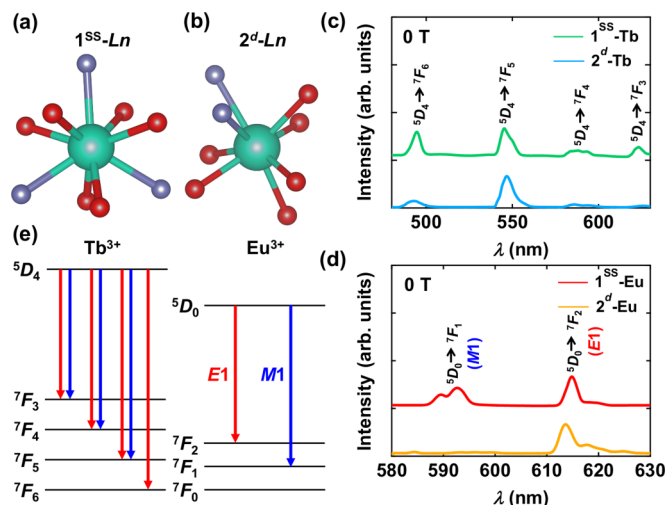

FIG. 3. The atomic coordination structures in the first coordination area around lanthanide ions (Ln^{3+}) and luminescence spectra of them. The atomic coordination structures in the first coordination area around Ln^{3+} in (a) $\mathbf{1^{SS}}$-Ln and (b) $\mathbf{2^d}$-Ln. Luminescence spectra of (c) $\mathbf{1^{SS}}$-**Tb** at 5 K and $\mathbf{2^d}$-**Tb** at 4.3 K in $H = 0$ T and (d) $\mathbf{1^{SS}}$-**Eu** at 5 K and $\mathbf{2^d}$-**Eu** at 4.2 K in $H = 0$ T. $E1$ and $M1$ represent an electric dipole active and a magnetic dipole active transitions, respectively. (e) Schematic figures of light emission processes in Tb^{3+} and Eu^{3+} ions. The red and blue arrows represent $E1$ and $M1$ transitions, respectively. In Tb^{3+}, within the approximation of the selection rules, $^5D_4 \to {}^7F_J$ ($J = 3,\ 4,\ 5$) are both active for $E1$ and $M1$ transitions. $^5D_4 \to {}^7F_6$ is only active for $E1$ transition. In europium(III), within the approximation of the selection rules, $^5D_0 \to {}^7F_1$ and $^5D_0 \to {}^7F_2$ are only active for $M1$ and $E1$ transitions, respectively.

paramagnetic moment [Fig. 2(a)]. The χT values of $\mathbf{1^{SS}}$-**Tb** and $\mathbf{1^{SS}}$-**Eu** at 300 K are 11.56 cm³ and 0.84 cm³ K mol⁻¹, respectively [Fig. 2(b)]. Compound $\mathbf{1^{SS}}$-**Tb** exhibits a Curie constant value close to 11.82 cm³ K mol⁻¹ for the magnetic moment of $J = 6$ in Tb^{3+} ($^7F_6$), which is calculated by using the Landé g factor, $g = 3/2$. Since the ground state of Eu^{3+} is nonmagnetic with $J = 0$ ($^7F_0$), the observed small and temperature independent paramagnetic moment in $\mathbf{1^{SS}}$-**Eu** could be ascribed to the Van Vleck paramagnetism, which is induced by mixing the excited paramagnetic states of $J \neq 0$ to the nonmagnetic ground state of $J = 0$ in the magnetic field.

C. Luminescence spectroscopy

Figures 3(c) and 3(d) display the luminescence spectra of $\mathbf{1^{SS}}$-/$\mathbf{2^d}$-**Tb** and $\mathbf{1^{SS}}$-/$\mathbf{2^d}$-**Eu** at 0 T, respectively. The excitation for luminescence was carried out by irradiating a UV light ($\lambda \leqslant 400$ nm) corresponding to a characteristic band for the ligand $L^{SS/RR}$ (Fig. S6 in the Supplemental Material), d/l-tfc, and phen, which enable the mediation of photon energy transfer to Tb^{3+}/Eu^{3+}. The visible light emission developed in both $\mathbf{1^{SS}}$-**Tb** and $\mathbf{1^{SS}}$-**Eu** by measuring at a low temperature of 77 K, rather than at room temperature (Fig. S7 in the Supplemental Material). Comparing the lumi-

nescence spectra of $\mathbf{1^{SS}}$-**Tb**/$\mathbf{1^{SS}}$-**Eu** in methanol and PMMA, the effect of the matrix was hardly observed (Fig. S8 in the Supplemental Material). Four luminescence bands for $\mathbf{1^{SS}}$-**Tb** ($\lambda_6 \sim 495$, $\lambda_5 \sim 545$, $\lambda_4 \sim 590$, and $\lambda_3 \sim 620$ nm) and two luminescence bands for $\mathbf{1^{SS}}$-**Eu** ($\lambda_1 \sim 595$ and $\lambda_2 \sim 615$ nm) were observed with fine structures related to the crystal-field splitting [Figs. 3(c) and 3(d)], which were assigned to the f–f transitions of $^5D_4 \to {}^7F_J$ ($J = 6, 5, 4, 3$) in Tb^{3+}, and those of $^5D_0 \to {}^7F_J$ ($J = 1,\ 2$) in Eu^{3+}, respectively [Fig. 3(e)] [36]. In a noncentrosymmetric crystal field, the selection rule for electric dipole ($E1$) transition of f electrons between J and J' states in a lanthanide ion is given by the Judd-Ofelt theory: $|\Delta J| \equiv |J' - J| \leqslant 6$ for J and $J' \neq 0$, and $|\Delta J| = 2, 4, 6$ for J or $J' = 0$ [37,38]. On the other hand, the selection rule for magnetic dipole ($M1$) transition is $\Delta J = \pm 1, 0$ except for the case $J = J' = 0$, which is the forbidden process [39]. Based on these selection rules, in Tb^{3+}, the $^5D_4 \to {}^7F_6$ transitions are the only $E1$ allowed process and the $^5D_4 \to {}^7F_J$ ($J = 5, 4, 3$) transitions are both $E1$ and $M1$ allowed processes [Fig. 3(e)]. In Eu^{3+}, $^5D_0 \to {}^7F_1$ and $^5D_0 \to {}^7F_2$ transitions are the only $M1$ allowed process and the only $E1$ allowed process, respectively [Fig. 3(e)]. For these luminescence bands, the circularly polarized luminescence (CPL) was measured to confirm the chiral environments at the Ln coordinating sites in $\mathbf{1^{SS/RR}}$-**Tb** and $\mathbf{1^{SS/RR}}$-**Eu** (Fig. S9 in the Supplemental Material).
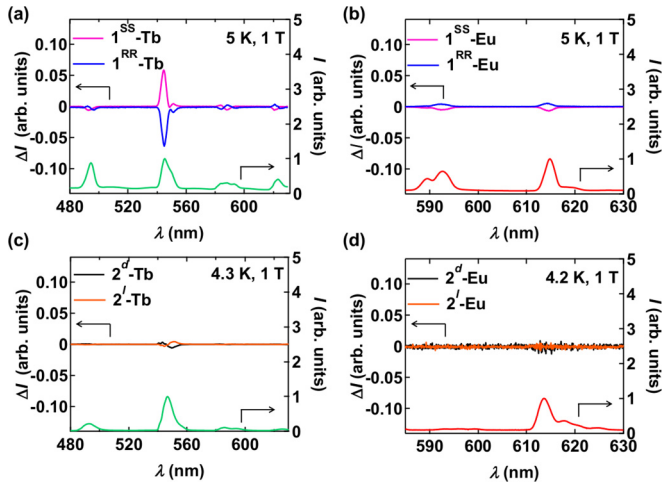
FIG. 4. MChD spectra of (a) **1$^{SS/RR}$-Tb**, (b) **1$^{SS/RR}$-Eu**, (c) **2$^{d/l}$-Tb**, (d) **2$^{d/l}$-Eu** at $H = 1$ T, where $\Delta I \equiv I(+1\,\mathrm{T}) - I(-1\,\mathrm{T})$, and the averaged luminescence spectra of (a) **1^{SS}-Tb**, (b) **1^{SS}-Eu**, (c) **2^d-Tb**, (d) **2^d-Eu** at $H = 1$ T, where $I \equiv \{I(+1T) + I(-1T)\}/2$. MChD spectra of **1^{SS}-Ln** and **1^{RR}-Ln** at 1 T are represented by pink and blue lines, respectively. MChD spectra of **2^d-Ln** and **2^l-Ln** at 1 T are represented by black and orange lines, respectively. The spectral intensities are normalized by the maximum values of each luminescence spectrum.

D. MChD for luminescence in the visible light region

The luminescence measurements under magnetic fields (**H**) for the detection of MChD were conducted in a Faraday configuration, in which **H** was applied parallel or antiparallel to the emitted light propagating vector (**k**) (Fig. S5 in the Supplemental Material). By reversing the direction of **H**, while keeping the **k** direction fixed, the relative direction of **k** to **H**, **k · H**, is switched between parallel and antiparallel configurations. Figures 4(a) and 4(b) show the luminescence spectra (*I*) in the magnetic field and the difference spectra of the luminescence intensity (*ΔI*) between the opposite directions of **H**, namely, $H = \pm 1$ T at 5 K for **1$^{SS/RR}$-Tb** and **1$^{SS/RR}$-Eu**, respectively. *I* and *ΔI* are defined as the averaged luminescence intensity under a magnetic field $\pm H$ (i.e., $I \equiv \{I(+H) + I(-H)\}/2$) and the change in the luminescence intensity with the reversal of **H** (i.e., $\Delta I \equiv I(+H) - I(-H)$), respectively. In the luminescence difference spectra of both **1^{SS}-Tb** and **1^{SS}-Eu**, nonzero *ΔI* signals clearly appear, indicating the **k · H** dependence of luminescence intensity. In addition, the sign reversal of *ΔI* was demonstrated in the enantiomer pairs of Tb^{3+} and Eu^{3+} (**1^{SS}-Tb/1^{RR}-Tb** and **1^{SS}-Eu/1^{RR}-Eu**). These MChD detections were confirmed in all the transitions $^5D_4 \rightarrow ^7F_J$ ($J = 6, 5, 4, 3$) in Tb^{3+} (**1$^{SS/RR}$-Tb**) and $^5D_0 \rightarrow ^7F_J$ ($J = 1, 2$) in Eu^{3+} (**1$^{SS/RR}$-Eu**). Importantly, the MChD is much stronger in the Tb^{3+} system than the Eu^{3+} system [Figs. 4(a) and 4(b)]. The maximum peak magnitudes of $\Delta I/I$ at $H = 1$ T in **1$^{SS/RR}$-Tb** and **1$^{SS/RR}$-Eu** are about 6×10^{-2} (∼6%) and 3×10^{-3} (∼0.3%), respectively. For comparison, we also measured MChD for the Eu^{3+} complex [Eu(d-tfc)$_3$] (d-tfc = 3-trifluoroacetyl-d-camphorato), reported previously by Rikken *et al.* [8] at similar condition with **1$^{SS/RR}$-Tb/Eu** (at $H = 1$ T and $T = 4.2$ K).
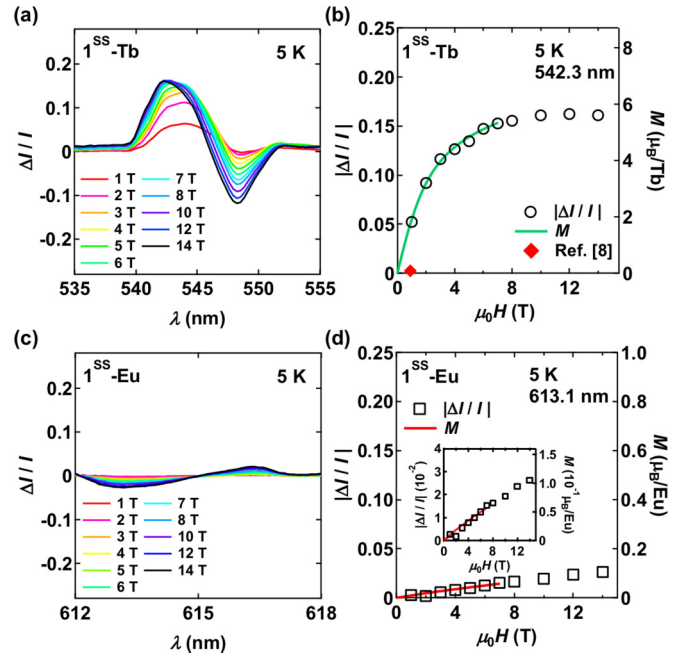

FIG. 5. Magnetic field dependence of MChD signal in luminescence. (a) Magnetic field dependence of MChD spectra of **1^{SS}-Tb** at 5 K. The $^5D_4 \rightarrow ^7F_5$ band, which shows the strongest MChD signal in **1^{SS}-Tb**, is displayed. (b) Magnetic field dependence of $|\Delta I/I|$ at 542.3 nm (open circles) and magnetization (*M*) of **1^{SS}-Tb** (green line) at 5 K. The red diamond represents the previously reported maximum luminescence MChD signal for the visible light region in the literature (Ref. [8]). (c) Magnetic field dependence of MChD spectra of **1^{SS}-Eu** at 5 K. The $^5D_0 \rightarrow ^7F_2$ band is displayed. (d) Magnetic field dependence of $|\Delta I/I|$ at 613.1 nm (open squares) and *M* of **1^{SS}-Eu** (red line) at 5 K. The inset displays the magnified figure.

However, the *ΔI* value could not be detected (Fig. S10 in the Supplemental Material), possibly due to a detection limit of the present nonphase-sensitive method using a DC magnetic field (Fig. S5 in the Supplemental Material).

Figure 5(a) shows the magnetic field dependence of the normalized MChD signal ($\Delta I/I$) at 5 K for $^5D_4 \rightarrow ^7F_5$ with the strongest MChD intensity in **1^{SS}-Tb** (the spectra for the whole wavelength range is displayed in Fig. S11 in the Supplemental Material). The magnitude of the MChD signal develops with increasing *H* and Fig. 5(b) depicts a plot of $\Delta I/I$ at 542.3 nm vs *H* for **1^{SS}-Tb**. The MChD signal of **1^{SS}-Tb** gradually increases and almost saturates at $H \sim 10$ T. At $H = 14$ T, the MChD signal reaches up to about 0.16 (∼16%) of the corresponding luminescence intensity. Notably, this *H* dependence of $\Delta I/I$ follows the *H* dependence of the magnetization (*M*) for **1^{SS}-Tb**, i.e., Brillouin function-like paramagnetic behavior of Tb^{3+}-centered complex with $J = 6$ [green line of Fig. 5(b)]. The MChD is microscopically described as an interference effect between electric dipole ($E1$) and magnetic dipole ($M1$) transitions in the ultraviolet-visible-infrared light region [7,17,19] (See Appendix A). From the microscopic viewpoint, the *H* dependence of MChD signals on the $f-f$ emissions originates from *J*-multiplet states ($M_J = J, J-1, \cdots, -J+1, -J$) involving in the light emission process as the initial/final state [7]. These *J*-multiplet states

should be reflected in MChD signals through the occupancy distribution in their Zeeman splitting $(2J + 1)$ state, as in the generation of magnetization, because the MChD signals from the two states with opposite sign of M_J cancel out each other (See Appendix B). Considering that the ground state of Tb^{3+} ($^7F_6$), which gives the magnetization, is not the final state in the now focused luminescence band in Fig. 5(a) ($^5D_4 \rightarrow {}^7F_5$) [Fig. 3(e)], the origin of the saturating H dependence of the M-like MChD signal seems to be ascribed to occupancy distribution of the excited light emission state ($^5D_4$) with nonzero J value ($J = 4$). It might be correlated with that of the ground state ($^7F_6$) in the energy transfer process from antenna ligands, L^{SS}, to Tb^{3+} [36]. The similar H dependence of the MChD signal with M is also observed in the Eu^{3+} system (**1^{SS}-Eu**) [Figs. 5(c) and 5(d)]. Also in the Eu^{3+} system, since the ground state of Eu^{3+} ($^7F_0$) is not the final state in the focused luminescence band in Fig. 5(c) ($^5D_0 \rightarrow {}^7F_2$) [Fig. 3(e)], the similar H dependence of the MChD signal with M, which reflects the nonmagnetic ground state ($^7F_0$ with $J = 0$), might arise from the nonmagnetic excited light emission state ($^5D_0$ with $J = 0$). In the nonmagnetic state of $J = 0$ without electronic states mixing, since no Zeeman splitting is induced by the magnetic field, the intensity of the MChD signal should be suppressed.

The observation of strong MChD of **1$^{SS/RR}$-Tb** is thus partly due to the contribution of the occupancy distribution of the Zeeman splitting states produced by M_J of the Tb^{3+} ion with $J \neq 0$, but it should also be associated with the symmetrical nature of local coordination geometry around the Tb^{3+} ion. The isostructural series $[Ln(d/l\text{-tfc})_3(\text{phen})]$ ($Ln =$ Tb, **2$^{d/l}$-Tb**; Eu, **2$^{d/l}$-Eu**) has a distorted octa-coordinated geometry with three chiral O;O bidentate d/l-tfc ligands and one N;N bidentate phen ligand [Figs. 1(c) and 3(b)], the local crystal field potential at the Ln^{3+} site for which should be greatly deformed from that in **1$^{SS/RR}$-Tb/Eu** [Figs. 1(b) and 3(a)]. The maximum peak value of $\Delta I/I$ for **2$^{d/l}$-Tb** at $H = 1$ T is about $1–2 \times 10^{-2}$ (1–2%) [Fig. 4(c)], while that for **2$^{d/l}$-Eu** was hardly observed [Fig. 4(d)]. Thus, the integrated intensity of $|\Delta I/I|$ at each band of **2$^{d/l}$-Tb** is much smaller than that in **1$^{SS/RR}$-Tb**. The magnetization value of **2^d-Tb** at $H = 1$ T is similar to that of **1^{SS}-Tb** (Fig. S12 in the Supplemental Material), indicating that the stronger MChD intensity in **1^{SS}-Tb** than **2^d-Tb** is not ascribed to the difference of magnetization. So, the intensity difference of MChD signals between these Tb^{3+} complexes could be attributed to the difference of the first coordination area around Tb^{3+}: the degree of the inversion symmetry breaking at the Tb^{3+} site (*vide infra*).

In the microscopic description based on the $E1$-$M1$ interference mechanism, the magnitude of MChD ($|\Delta I/I|$) should be maximized when the $M1$ transition is the same degree as the $E1$ transition, i.e., $|M1| = |E1|$ (See Appendix A) [31], while a number of electronic transitions, such as charge transfer transition between metal and ligands and π-π^* transition in chiral transition metal complexes, have the relationship $|E1| \gg |M1|$, which is a disadvantage for strong MChD. Here, $|E1|$ and $|M1|$ represent the magnitude of $E1$ transition and $M1$ transition, respectively.

Meanwhile, in the case of f–f transitions in chiral lanthanide complexes, the $M1$ transition is fully allowed, whereas

the $E1$ transition is weakly allowed by a noncentrosymmetric crystal field, i.e., possibly allowing a situation closer to the favorable condition for strong MChD; $|M1| \approx |E1|$. This is one of the critical reasons why chiral lanthanide complexes were chosen in Rikken's first report [8] and in this work. However, even in inversion symmetry-broken chiral f-orbital metal complexes, the deviation from the centrosymmetric crystal field around a metal ion remains as a tunable key factor to modulate the $E1$ transition strength. In the f–f transitions of lanthanide complexes, we can experimentally evaluate the degree of inversion symmetry breaking at the lanthanide site through a comparison of the luminescence spectra of Eu complexes **1^{SS}-Eu** and **2^d-Eu**, which exhibit two characteristic bands of $^5D_0 \rightarrow {}^7F_1$ ($\sim$595 nm) and $^5D_0 \rightarrow {}^7F_2$ ($\sim$615 nm) [Fig. 3(d)], corresponding to $M1$- and $E1$-allowed processes, respectively [Figs. 3(d) and 3(e)] [37–39]. Because the $M1$ transition is independent of the inversion symmetry breaking, the ratio of the spectral intensities between the $^5D_0 \rightarrow {}^7F_2$ ($E1$) and the $^5D_0 \rightarrow {}^7F_1$ ($M1$) transitions, $R \equiv I(^5D_0 \rightarrow {}^7F_2)/I(^5D_0 \rightarrow {}^7F_1)$, is often used for understanding the degree of inversion symmetry breaking at the Eu^{3+} site [40]. The R value of **1^{SS}-Eu**($R \sim 1.0$) is much smaller than that of **2^d-Eu**($R \sim 13.6$) [Fig. 3(d)], indicating that **1^{SS}-Eu** has an environment with smaller inversion symmetry breaking (i.e., relatively higher symmetry) at the Eu^{3+} site than **2^d-Eu**. Considering the isostructural forms of the corresponding Tb^{3+} complexes (Fig. S4 in the Supplemental Material), the symmetry breaking at the Tb^{3+} site in **1^{SS}-Tb** could be smaller than in **2^d-Tb**: **1^{SS}-Tb** has a relatively higher symmetrical geometry around the Tb^{3+} center than **2^d-Tb**. Thus, the $E1$ transition is suppressed in **1^{SS}-Tb**: this situation is much closer to the ideal relationship for strong MChD; $|M1| \approx |E1|$. In fact, reflecting this situation, the strength of MChD of **1^{SS}-Tb** is remarkably improved compared with that of **2^d-Tb** [Figs. 4(a) and 4(c)]. Consequently, the duplicate effects of (i) $J \neq 0$ and (ii) smaller inversion-symmetry breaking at the Ln center, which are adequate only for **1^{SS}-Tb**, were effective for the observation of strong MChD.

IV. SUMMARY

In summary, strong MChD for light emissions in the visible light region was detected in the chiral Tb^{3+} complex **1^{SS}-Tb**, which reaches approximately 16% of the luminescence intensity at $H = 14$ T with developing magnetization. In addition to the advantage of a large magnetic moment with the $J \neq 0$ state, the degree of inversion symmetry breaking at the Ln metal coordinating area is very important to gain stronger MChD signals. These clear strategies, (i) $J \neq 0$ and (ii) smaller inversion symmetry breaking at the Ln center (i.e., the symmetry of a first coordination area), may lead to the design principles of chiral Ln complexes exhibiting much stronger MChD.

APPENDIX A: MICROSCOPIC DESCRIPTION OF MChD

From the microscopic viewpoints, MChD is described as the interference effect between electric dipole ($E1$) and either magnetic dipole ($M1$) or electric quadrupole ($E2$) transitions [7,19]. In particular, in the ultraviolet-visible-infrared light region, on which we are now focusing, the $E1$–$M1$ interference term is considered to be dominant [17]. In such a situation, according to Fermi's golden rule, the light emission intensity I_+ and I_- for opposite propagating direction to the magnetic field are expressed as

$$
\begin{aligned}
I_{\pm} &\propto |\langle f|H_{E1} \pm H_{M1}|i\rangle|^2 \\
&= |\langle f|H_{E1}|i\rangle|^2 + |\langle f|H_{M1}|i\rangle|^2 \\
&\pm (\langle i|H_{E1}|f\rangle\langle f|H_{M1}|i\rangle + \text{c.c.}).
\end{aligned} \tag{A1}
$$

Here, $|i\rangle$ and $|f\rangle$ stand for the initial and the final states in the optical transition, respectively. H_{E1} and H_{M1} are the operators of the electric dipole and the magnetic dipole interaction in electromagnetic radiation, respectively. c.c. represents the conjugate complex. $|\langle f|H_{E1}|i\rangle|^2$ and $|\langle f|H_{M1}|i\rangle|^2$ are proportional to the probability of $E1$ and $M1$ transitions, respectively. From Eq. (A1), the intensity of MChD signal, $\Delta I \equiv I_+ - I_-$, is described as

$$
\Delta I \equiv I_+ - I_- \propto 2(\langle i|H_{E1}|f\rangle\langle f|H_{M1}|i\rangle + \text{c.c.}). \tag{A2}
$$

As displayed in Eq. (A2), the magnitude of MChD is given by the interference terms of the $E1$ and the $M1$ transitions: $\langle i|H_{E1}|f\rangle\langle f|H_{M1}|i\rangle$ or $\langle i|H_{E1}|f\rangle^*\langle f|H_{M1}|i\rangle^*$. These interference terms can only appear in noncentrosymmetric systems, such as chiral and polar materials, because the parity of H_{E1} and H_{M1} are different: H_{E1} and H_{M1} have odd and even parity, respectively.

The signal strength of nonreciprocal directional dichroism, such as MChD, is usually compared using the normalized one by the averaged luminescence intensity ($I \equiv (I_+ + I_-)/2$) [8], which is defined as

$$
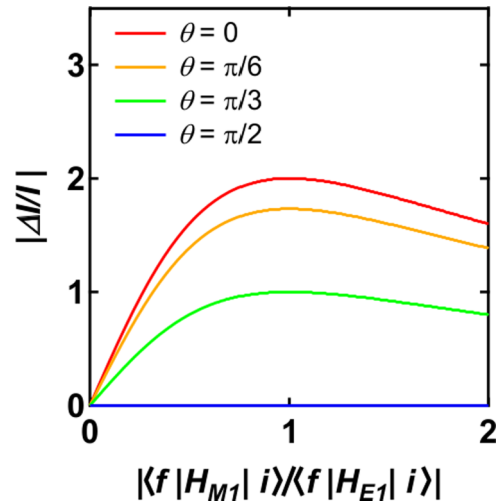\frac{\Delta I}{I} \equiv \frac{I_+ - I_-}{\frac{1}{2}(I_+ + I_-)}. \tag{A3}
$$

FIG. 6. Simulation of $|\Delta I/I|$ calculated by Eq. (A5). The θ is a phase defined by the following formula: $\langle i|H_{M1}|f\rangle/\langle f|H_{E1}|i\rangle = r\exp(i\theta)$. r is the amplitude of $\langle i|H_{M1}|f\rangle/\langle f|H_{E1}|i\rangle$; $r = |\langle i|H_{M1}|f\rangle/\langle f|H_{E1}|i\rangle|$.

From Eqs. (A1) and (A2), the normalized strength of MChD, $\Delta I/I$, is expressed as

$$
\begin{aligned}
\frac{\Delta I}{I} &= \frac{2(\langle i|H_{E1}|f\rangle\langle f|H_{M1}|i\rangle + \langle i|H_{E1}|f\rangle^*\langle f|H_{M1}|i\rangle^*)}{|\langle f|H_{E1}|i\rangle|^2 + |\langle f|H_{M1}|i\rangle|^2} \\
&= \frac{2\left(\frac{\langle f|H_{M1}|i\rangle}{\langle f|H_{E1}|i\rangle} + \frac{\langle f|H_{M1}|i\rangle^*}{\langle f|H_{E1}|i\rangle^*}\right)}{1 + \left|\frac{\langle f|H_{M1}|i\rangle}{\langle f|H_{E1}|i\rangle}\right|^2} \\
&= \frac{4\mathrm{Re}\left(\frac{\langle f|H_{M1}|i\rangle}{\langle f|H_{E1}|i\rangle}\right)}{1 + \left|\frac{\langle f|H_{M1}|i\rangle}{\langle f|H_{E1}|i\rangle}\right|^2}.
\end{aligned} \tag{A4}
$$
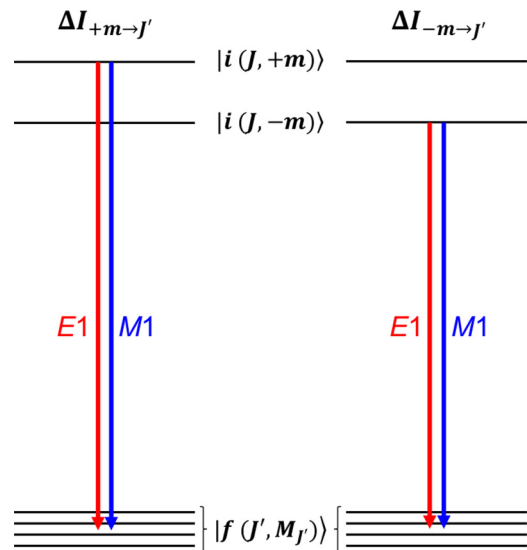

FIG. 7. Schematic figure of the electronic transition of MChD for $\Delta I_{+m\to J'}$ and $\Delta I_{-m\to J'}$. In the initial state, $|i(J, M_J)\rangle$, the M_J states other than those of $\pm m$ are omitted for clarity.

Here, we set $\langle i|H_{M1}|f\rangle/\langle f|H_{E1}|i\rangle = r\exp(i\theta)$ and express $\Delta I/I$ as a function of r $(=|\langle i|H_{M1}|f\rangle/\langle f|H_{E1}|i\rangle|)$ and θ; $f(r,\theta)$:

$$\frac{\Delta I}{I} = f(r,\theta) = \frac{4r\cos\theta}{1+r^2}. \tag{A5}$$

From the condition that $\frac{\partial f(r,\theta)}{\partial r} = 0$ and $\frac{\partial f(r,\theta)}{\partial \theta} = 0$, we find that $f(r,\theta)$ takes the maximum value ($f^{\text{MAX}} = 2$) for $r = 1$, $\theta = 0$, and the minimum value ($f^{\text{MIN}} = -2$) for $r = 1$, $\theta = \pi$. Thus, the normalized magnitude of MChD,

$|\Delta I/I|$, becomes maximum when $|\langle f|H_{E1}|i\rangle| = |\langle f|H_{M1}|i\rangle|$ (Fig. 6). However, in most materials, since the $E1$ transition moment is much stronger than the $M1$ transition moment, $|\langle f|H_{E1}|i\rangle| \gg |\langle f|H_{M1}|i\rangle|$, the signal of MChD becomes very weak, $|\Delta I/I| \to 0$ (Fig. 6).

On the other hand, in a chiral lanthanide complex, the $f-f$ transitions, in which the $M1$ transition is fully allowed and the $E1$ transition is weakly allowed by a noncentrosymmetric crystal field, are promising candidates for observing strong MChD because the comparable $E1$ transition and the $M1$ transition moments are potentially realized.

APPENDIX B: RELATIONSHIP BETWEEN MChD SIGNAL AND MAGNETIZATION

In lanthanide complexes, a magnetic field lifts the $(2J+1)$ degeneracy of each J multiplet of lanthanide ion via Zeeman energy. In the case where the energy of Zeeman splitting is smaller than the energy width of each luminescence band, the MChD signal from the $J \to J'$ transition, $\Delta I_{J \to J'}$, should be observed as one band peak and the intensity of $\Delta I_{J \to J'}$ should be approximately given by the summation of the MChD signals from the all splitting $(2J+1)$ states; $M_J = J, J-1, J-2 \cdots - J+2, -J+1, -J$. In particular, since the MChD signal from the $M_J = +m$ state ($\Delta I_{+m \to J'}$) as an initial state cancels out that from the $M_J = -m$ state ($\Delta I_{-m \to J'}$) ($m = J, J-1, J-2 \cdots \geqslant 0$), the occupancy distribution for the Zeeman splitting states, which produces magnetization, is necessary for observation of MChD (*vide infra*). The correlation between a MChD signal and a magnetization would arise from the occupancy distribution for the Zeeman splitting states in a paramagnetic material with $J \neq 0$.

The relationship between $\Delta I_{+m \to J'}$ and $\Delta I_{-m \to J'}$ is given by introducing a time reversal symmetry operator, $\hat{\Theta}$. From Eq. (1), $\Delta I_{+m \to J'}$ and $\Delta I_{-m \to J'}$ (Fig. 7) are expressed as

$$\Delta I_{+m \to J'} = A \sum_{M_{J'}=-J'}^{+J'} (|\langle f(J',M_{J'})|H_{E1}+H_{M1}|i(J,+m)\rangle|^2 - |\langle f(J',M_{J'})|H_{E1}-H_{M1}|i(J,+m)\rangle|^2), \tag{B1}$$

$$\Delta I_{-m \to J'} = A \sum_{M_{J'}=-J'}^{+J'} (|\langle f(J',M_{J'})|H_{E1}+H_{M1}|i(J,-m)\rangle|^2 - |\langle f(J',M_{J'})|H_{E1}-H_{M1}|i(J,-m)\rangle|^2). \tag{B2}$$

Here, A is a constant of proportionality in Eq. (A1). We express the $\hat{\Theta}$-applied initial state and final state as $|\tilde{i}\rangle = \hat{\Theta}|i\rangle$ and $|\tilde{f}\rangle = \hat{\Theta}|f\rangle$, respectively. Using these expressions, Eq. (B1) is written as

$$\Delta I_{+m \to J'} = A \sum_{M_{J'}=-J'}^{+J'} (|\langle f(J',M_{J'})|H_{E1}+H_{M1}|i(J,+m)\rangle|^2 - |\langle f(J',M_{J'})|H_{E1}-H_{M1}|i(J,+m)\rangle|^2)$$

$$= A \sum_{M_{J'}=-J'}^{+J'} (|\langle \tilde{f}(J',M_{J'})|\hat{\Theta}(H_{E1}+H_{M1})\hat{\Theta}^{-1}|\tilde{i}(J,+m)\rangle^*|^2 - |\langle \tilde{f}(J',M_{J'})|\hat{\Theta}(H_{E1}-H_{M1})\hat{\Theta}^{-1}|\tilde{i}(J,+m)\rangle^*|^2)$$

$$= A \sum_{M_{J'}=-J'}^{+J'} (|\langle \tilde{f}(J',M_{J'})|H_{E1}-H_{M1}|\tilde{i}(J,+m)\rangle^*|^2 - |\langle \tilde{f}(J',M_{J'})|H_{E1}+H_{M1}|\tilde{i}(J,+m)\rangle^*|^2)$$

$$= A \sum_{M_{J'}=-J'}^{+J'} (|\langle f(J',-M_{J'})|H_{E1}-H_{M1}|i(J,-m)\rangle^*|^2 - |\langle f(J',-M_{J'})|H_{E1}+H_{M1}|i(J,-m)\rangle^*|^2)$$

$$= -A \sum_{M_{J'}=-J'}^{+J'} (|\langle f(J',M_{J'})|H_{E1}+H_{M1}|i(J,-m)\rangle|^2 - |\langle f(J',M_{J'})|H_{E1}-H_{M1}|i(J,-m)\rangle|^2)$$

$$= -\Delta I_{-m \to J'}. \tag{B3}$$

Here, we use the relationship that $H_{E1}{}^{\dagger} = H_{E1}$, $H_{M1}{}^{\dagger} = H_{M1}$, $\hat{\Theta}H_{E1}\hat{\Theta}^{-1} = H_{E1}$, $\hat{\Theta}H_{M1}\hat{\Theta}^{-1} = -H_{M1}$, and the characteristic of $\hat{\Theta}$ as an antiunitary operator. From Eq. (B3), we can confirm that the MChD signal from the $M_J = +m$ state and that from the $M_J = -m$ state cancel out each other ($\Delta I_{+m \to J'} + \Delta I_{-m \to J'} = 0$). Thus, asymmetric occupancy distribution between $M_J = +m$ and $M_J = -m$ states is necessary for the appearance of MChD.

[1] S. F. Mason, in Circular Dichroism*: Principles and Applications* edited by K. Nakanishi, N. Berova, and R. W. Woody (VCH, New York, 1994), Chap. 2.

[2] L. D. Barron, Nature (London) **405**, 895 (2000).

[3] G. L. J. A. Rikken, Science **331**, 864 (2011).

[4] J. R. Galán-Mascarós, Nat. Phys. **11**, 7 (2015).

[5] S. Mühlbauer, B. Binz, F. Jonietz, C. Pfleiderer, A. Rosch, A. Neubauer, R. Georgii, and P. Böni, Science **323**, 915 (2009).

[6] B. Göhler, V. Hamelbeck, T. Z. Markus, M. Kettner, G. F. Hanne, Z. Vager, R. Naaman, and H. Zacharias, Science **331**, 894 (2011).

[7] L. D. Barron and J. Vrbancich, Mol. Phys. **51**, 715 (1984).

[8] G. L. J. A. Rikken and E. Raupach, Nature (London) **390**, 493 (1997).

[9] C. Train, R. Gheorghe, V. Krstic, L.-M. Chamoreau, N. S. Ovanesyan, G. L. J. A. Rikken, M. Gruselle, and M. Verdaguer, Nat. Mater. **7**, 729 (2008).

[10] Y. Kitagawa, H. Segawa, and K. Ishii, Angew. Chem. Int. Ed. **50**, 9133 (2011).

[11] Y. Kitagawa, T. Miyatake, and K. Ishii, Chem. Commun. **48**, 5091 (2012).

[12] K. Wang, S. Zeng, H. Wang, J. Dou, and J. Jianzhuang, Inorg. Chem. Front. **1**, 167 (2014).

[13] S. Eslami, J. G. Gibbs, Y. Rechkemmer, J. Slageren, M. Alarcón-Correa, T.-C. Lee, A. G. Mark, G. L. J. A. Rikken, and P. Fischer, ACS Photonics **1**, 1231 (2014).

[14] G. Kopnov and G. L. J. A. Rikken, Rev. Sci. Instrum. **85**, 053106 (2014).

[15] G. L. J. A. Rikken and E. Raupach, Phys. Rev. E **58**, 5081 (1998).

[16] M. Saito, K. Ishikawa, K. Taniguchi, and T. Arima, Phys. Rev. Lett. **101**, 117402 (2008).

[17] N. Nakagawa, N. Abe, S. Toyoda, S. Kimura, J. Zaccaro, I. Gautier-Luneau, D. Luneau, Y. Kousaka, A. Sera, M. Sera, K. Inoue, J. Akimitsu, Y. Tokunaga, and T. Arima, Phys. Rev. B **96**, 121102(R) (2017).

[18] M. Ceolín, S. Coberna-Ferrón, and J. R. Galán-Mascarós, Adv. Mater. **24**, 3120 (2012).

[19] R. Sessoli, M.-E. Boulon, A. Caneschi, M. Mannini, L. Poggini, F. Wilhelm, and A. Rogalev, Nat. Phys. **11**, 69 (2015).

[20] S. Bordács, I. Kézsmárki, D. Szaller, L. Demkó, N. Kida, H. Murakawa, Y. Onose, R. Shimano, T. Rõõm, U. Nagel, S. Miyahara, N. Furukawa, and Y. Tokura, Nat. Phys. **8**, 734 (2012).

[21] I. Kézsmárki, D. Szaller, S. Bordács, V. Kocsis, Y. Tokunaga, Y. Taguchi, H. Murakawa, Y. Tokura, H. Engelkamp, T. Rõõm and U. Nagel, Nat. Commun. **5**, 3203 (2014).

[22] Y. Takahashi, S. Kibayashi, Y. Kaneko, and Y. Tokura, Phys. Rev. B **93**, 180404(R) (2016).

[23] H. Narita, Y. Tokunaga, A. Kikkawa, Y. Taguchi, Y. Tokura, and Y. Takahashi, Phys. Rev. B **94**, 094433 (2016).

[24] S. Tomita, K. Sawada, A. Porokhnyuk, and T. Ueda, Phys. Rev. Lett. **113**, 235501 (2014).

[25] T. Kodama, S. Tomita, T. Kato, D. Oshima, S. Iwata, S. Okamoto, N. Kikuchi, O. Kitakami, N. Hosoito, and H. Yanagi, Phys. Rev. Appl. **6**, 024016 (2016).

[26] S. Tomita, H. Kurosawa, K. Sawada, and T. Ueda, Phys. Rev. B **95**, 085402 (2017).

[27] Y. Nii, R. Sasaki, Y. Iguchi, and Y. Onose, J. Phys. Soc. Jpn. **86**, 024707 (2017).

[28] Y. Okamura, F. Kagawa, S. Seki, M. Kubota, M. Kawasaki, and Y. Tokura, Phys. Rev. Lett. **114**, 197202 (2015).

[29] G. L. J. A. Rikken, and E. Raupach, Nature (London) **405**, 932 (2000).

[30] Y. Xu, G. Yang, H. Xia, G. Zou, Q. Zhang, and J. Gao, Nat. Commun. **5**, 5050 (2014).

[31] Y. Tokura, and N. Nagaosa, Nat. Commun. **9**, 3740 (2018).

[32] O. Kotova, J. A. Kitchen, C. Lincheneau, R. D. Peacock, and T. Gunnlaugsson, Chem. Eur. J. **19**, 16181 (2013).

[33] H. L. Goering, J. N. Eikenberry, G. S. Koermer, and C. J. Lattimer, J. Am. Chem. Soc. **96**, 1493 (1974).

[34] I. Ghosh, H. Zeng, and Y. Kishi, Org. Lett. **6**, 4715 (2004).

[35] T. Harada, H. Tsumatori, K. Nishiyama, J. Yuasa, Y. Hasegawa, and T. Kawai, Inorg. Chem. **51**, 6476 (2012).

[36] J. P. Leonard, and T. Gunnlaugsson, J. Fluoresc. **15**, 585 (2005).

[37] B. R. Judd, Phys. Rev. **127**, 750 (1962).

[38] G. S. Ofelt, J. Chem. Phys. **37**, 511 (1962).

[39] L. J. F. Broer, C. J. Gorter, and J. Hoogschagen, Physica **11**, 231 (1945).

[40] Y. Hasegawa, M. Yamamuro, Y. Wada, N. Kanehisa, Y. Kai, and S. Yanagida, J. Phys. Chem. A **107**, 1697 (2003).

[41] See Supplemental Material at http://link.aps.org/supplemental/10.1103/PhysRevMaterials.3.045202 for the detailed experimental methods, the crystal structures and basic physical characteristics of the samples, such as optical absorption spectra, circularly dichroism spectra, luminescence spectra, circularly polarized luminescence spectra and magnetization.